ADVANCED FUNCTIONAL MATERIALS
www.afm-journal.de

Check for updates

In Situ Observation of Point-Defect-Induced Unit-Cell-Wise Energy Storage Pathway in Antiferroelectric $PbZrO_3$

Xian-Kui Wei, Chun-Lin Jia, Krystian Roleder, Rafal E. Dunin-Borkowski, and Joachim Mayer*

Phase transition is established to govern electrostatic energy storage for antiferroelectric (AFE)-type dielectric capacitors. However, the source of inducing the phase transition and the pathway of storing the energy remains elusive so far given the ultrafast charging/discharging process under normal working conditions. Here, by slowing down the phase-transition speed using electron-beam irradiation as an external stimulus, the in situ dynamic energy-storage process in AFE $PbZrO_3$ is captured by using atomic-resolution transmission electron microscopy. Specifically, it is found that oxygen-lead-vacancy-induced defect core acts as a seed to initiate the antiferrodistortive-to-ferrodistortive transition in antiparallel-Pb-based structural frames. Associated with polarity evolution of the compressively strained defect core, the ferroelectric (FE)–ferrodistortive state expands bilaterally along the *b*-axis direction and then develops into charged domain configurations during the energy-storage process, which is further evidenced by observations at the ordinary FE states. With filling the gap of perception, the findings here provide a straightforward approach of unveiling the unit-cell-wise energy storage pathway in chemical defect-engineered dielectric ceramics.

1. Introduction

Dielectric capacitors, characteristic of ultrafast charging/discharging rate, high energy-storage density, voltage endurance, and good reliability, are receiving a great deal of attention for their potential applications in electronic devices and electrical power systems.[1] Towards further improving the recoverable energy density $U_e = \int EdP$ (**Figure 1**a), two complementary approaches are mainly implemented so far: the macroscopic one by developing novel material design strategies such as polymorphic nanodomain[2] and grain-orientation-engineered multilayers,[3] and the microscopic one by unveiling the energy-storage pathway and mechanism.[4,5] Obviously, in situ revealing the energy-storage pathway provides a fundamental perspective to elaborate the structure–property relationship. Nevertheless, the ultrafast charging and discharging processes, completed in milliseconds or less, in traditional parallel-plate capacitors (Figure 1a) bring great challenges to capture the transient transition between different phase states.[6–8]

Different from linear and ferroelectric (FE) dielectrics,[2,9] antiferroelectrics (AFEs) such as $PbZrO_3$ offer an appropriate prototype for unveiling the microscopic scale energy-storage process given its inherent coupling with the AFE-to-FE phase transition.[10–13] On the one hand, it is reported that the illumination electron beam in transmission electron microscopy (TEM) may act as an external stimulus to slow down the excitation and image the structural phase transition in real time.[14,15] This endows a possibility of probing the storage process of energy through atomic-resolution TEM imaging (Figure 1a). On the other hand, the small critical thickness (≈6.5 nm) provides a favorable condition for resolving the structural order parameters,[16,17] for example, tilting of oxygen octahedra,[18,19] and dynamically tracking their evolution during the AFE-to-FE transition. In addition, we find that the remnant polarization (P_r), ranging from ≈2.5 to 8.3 μC cm^{-2} in the polarization–electric field (P–E) double-hysteresis loop (Figure 1a and Figure S1, Supporting Information), is ubiquitous in pure and doped $PbZrO_3$,[12,20–22] $AgNbO_3$, and $NaNbO_3$.[23–25] As a factor of reducing the U_e, the inescapable P_r, irrelevant to antiparallel cation shifts with either complete or partial offset, motivates us to find out its relationship with the ubiquitous structural defects, for example, point and planar defects.[26–28]

Here, based on excitation of illumination electron beam,[14,29,30] we investigate in situ the impact of oxygen-lead-vacancy-induced defect structure on phase transitions of

Dr. X.-K. Wei, Prof. C.-L. Jia, Prof. R. E. Dunin-Borkowski, Prof. J. Mayer
Ernst Ruska-Centre for Microscopy and Spectroscopy with Electrons
Research Center Jülich
52425 Jülich, Germany
E-mail: x.wei@fz-juelich.de
Prof. C.-L. Jia
School of Microelectronics
Xi'an Jiaotong University
Xi'an 710049, China
Prof. K. Roleder
Institute of Physics
University of Silesia
Katowice 40007, Poland
Prof. J. Mayer
Gemeinschaftslabor für Elektronenmikroskopie (GFE) RWTH Aachen
Ahornstraße 55, 52074 Aachen, Germany
The ORCID identification number(s) for the author(s) of this article can be found under https://doi.org/10.1002/adfm.202008609.

© 2021 The Authors. Advanced Functional Materials published by Wiley-VCH GmbH. This is an open access article under the terms of the Creative Commons Attribution License, which permits use, distribution and reproduction in any medium, provided the original work is properly cited.

DOI: 10.1002/adfm.202008609

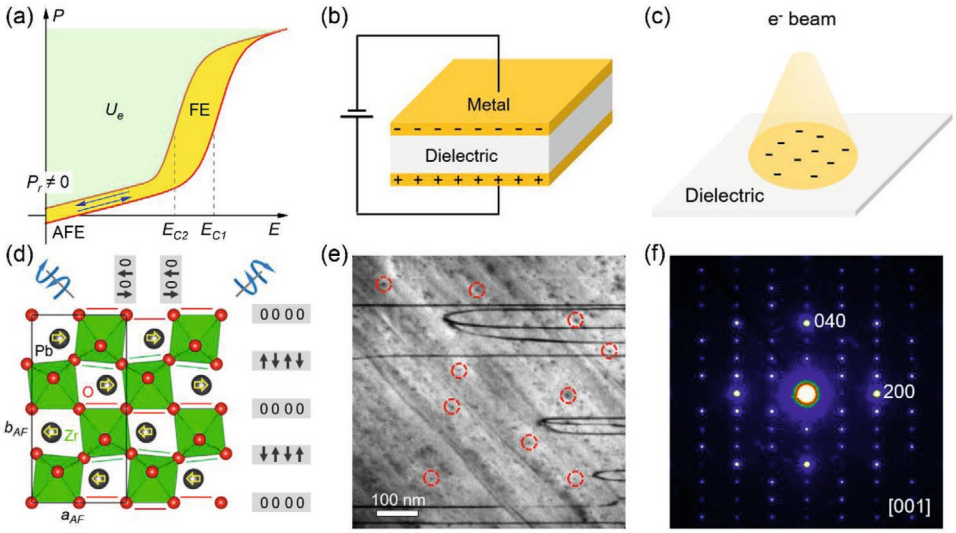

Figure 1. a) Schematic hysteresis loop at $E \geq 0$ with annotation of the recoverable energy-storage density U_e (green area) and coercive fields E_{C1} and E_{C2}. In real situations, the nonzero remnant polarization P_r at $E = 0$ usually broadens the linear region of the P–E loop. b) Typical capacitor geometry for electric-field biasing experiments. c) Illustration of electron-beam illumination as a stimulus for exciting and recording the structural phase transition. d) Crystal structure of AFE $PbZrO_3$ viewed along $[001]_O$ direction. The black arrows and zeros and line segments (red and green) characterize the AFD tilting of oxygen octahedra along the $x/[100]_O$ and $y/[010]_O$ direction, respectively. The empty yellow arrows denote antiparallel Pb shifts. e) Dark-field TEM image of $PbZrO_3$ recorded along $[001]_O$ with annotation of vacancy induced structural defects (red circles). f) Corresponding selected area electron diffraction (SAED) pattern taken along $[001]_O$ direction.

$PbZrO_3$ during energy storage in an image-corrected TEM. By simultaneously imaging light oxygen anions and heavy cations using negative spherical-aberration imaging (NCSI) technique,[17,31,32] our time-resolved dynamic study reveals that with retention of antiparallel Pb displacements, the vacancy-driven defect structure triggers an antiferrodistortive-to-ferrodistortive (AFD-to-FD) state transition in a stripe manner with variable width at unit-cell-wise level. Along with vanishing antiparallel Pb displacements, the FE/FD state instantly transforms into ordinary FE states. During the charge storage process, we also found presence and density increase of metastable charged domain walls. Our findings present a unit-cell-scale energy-storage pathway, which offers a strategy to expose atomic-scale energy storage process and structure–property relation in dielectric energy materials.

2. Results and Discussion

It is known that the orthorhombic AFE $PbZrO_3$ (space group *Pbam*) is characteristic of antiparallel Pb shifts along $[100]_O$ direction and antiphase rotations of oxygen octahedra along $[210]_O$ and $[\bar{2}10]_O$ direction ($a^-a^-c^0$ in Glaser's notation).[33,34] As viewed along $[001]_O$ direction, the oxygen atoms therefore undergo $(0 \uparrow 0 \downarrow)$ and $(0 \downarrow 0 \uparrow)$ shift behavior along $y/[010]_O$ direction and $(0 \leftarrow 0 \rightarrow)$ behavior along $x/[100]_O$ direction (Figure 1a and Figure S2a, Supporting Information). By carrying out thermal annealing treatments, that is, heating the specimen to a temperature slightly above T_C (≈500 K) and then cooling it down to room temperature, oxygen and Pb vacancies are successfully introduced into the lamella specimen (see Experimental Section). Observation of the intrinsic translational boundaries (dark-contrast straight lines in Figure 1a) and the structural modulation feature (Figure 1a) clearly evidence that the AFE phase is well maintained after the thermal treatment, where the lattice parameter ratio is measured as $b_{AF}/2a_{AF} = 0.995$.

In our experiments, a series of atomic-resolution TEM images were recorded from a vacancy-accumulating region using the NCSI technique along $[001]_O$ direction (**Figure 2**a). From a magnified central region of the initial AFE state ($t = -5$ s), we see that peak intensities of some oxygen columns (yellow dashed circles) are clearly reduced, which are accompanied with contrast enhancement of nearby Pb columns (green dashed squares, Figure 2a). By constructing different structural models, either surface or probability one, our multislice-based image simulations indicate that the oxygen and Pb vacancies, with reduction and increment on peak intensity, tend to locate on surfaces of the specimen (Figure 2a,d and Figure S3, Supporting Information). Through fitting peak positions of atomic columns using a 2D Gaussian function,[35] our mapping reveals a dislocation-free defect core, which is characteristic of vortex-like polar displacements of oxygen against centers of nearest-neighboring Zr columns (Figure 2a). Accordingly, a self-compensated polarization (P_S) configuration is formed inside the defect core, which resembles the topological domain states of $BaTiO_3$ as the FE nanorods are embedded in a $SrTiO_3$ matrix.[36,37]

Apart from breaking the AFD order of oxygen octahedra, we notice that the antiparallel Pb displacements near the defect core are also partially modified (Figure 2a and Figure S4a, Supporting Information). To understand the corresponding structural change, we further analyze local lattice deformation near the defect core using geometric phase analysis (GPA).[38] Referring to a region near the defect core, we see from the e_{xx} map that point vacancies lead to local lattice expansion along $[100]_O$

© 2021 The Authors. Advanced Functional Materials published by Wiley-VCH GmbH

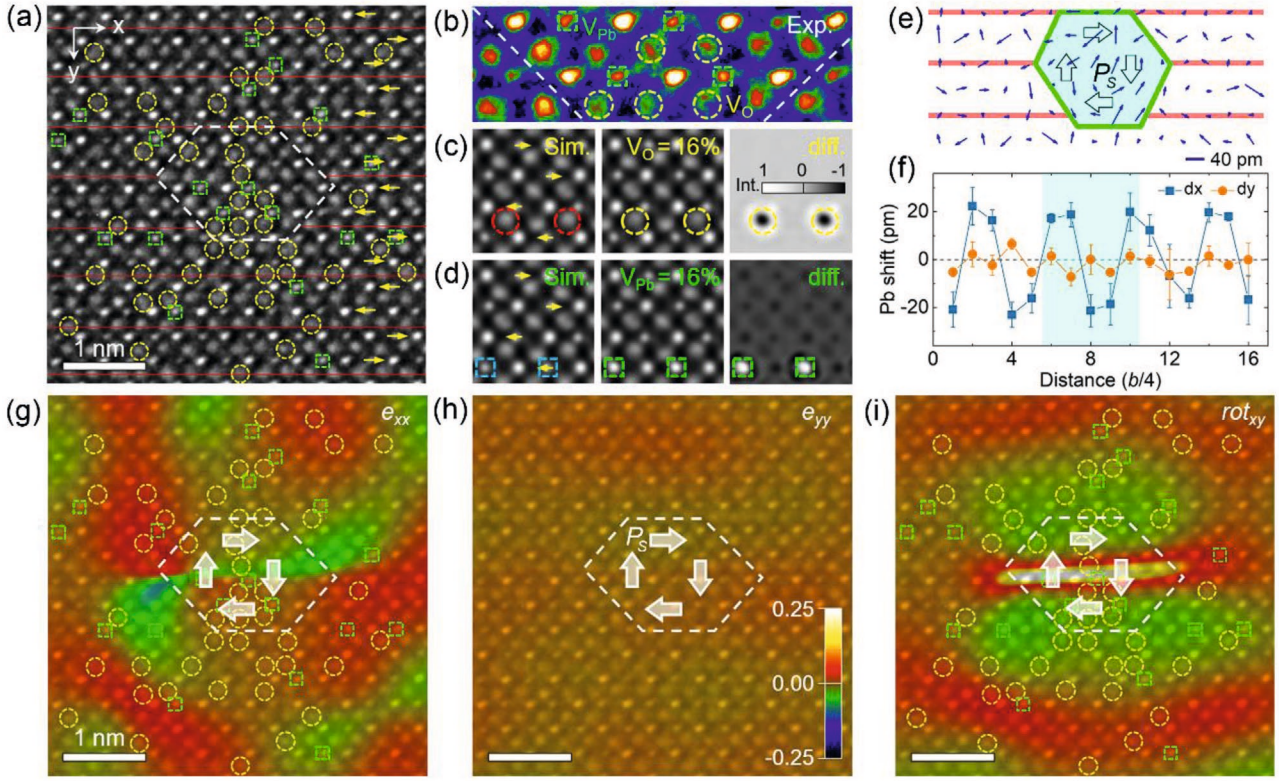

Figure 2. a) Atomic-resolution TEM image of the initial AFE phase (t = −5 s) along $[001]_O$ direction. The white dashed polygon, red solid lines, and yellow arrows denote the defect core, centrosymmetric oxygen sites, and antiparallel Pb shifts, respectively. b) Enlarged view of the vacancy-containing defect core. c,d) Simulated images of ideal (left panels) and vacancy-containing (middle panels) $PbZrO_3$ structure and their difference (right panels) for specimens with thickness = 10.2 nm and defocus = 8.5 nm. The vacancy concentration at specific columns is $V_O = V_{Pb}$ = 16%. e) Map of oxygen displacements near the defect core. f) Pb shifts along the $x//[100]_O$ and $y//[010]_O$ directions as a function of distance along y direction. g–i) Strain maps of e_{xx}, e_{yy}, and lattice rotation (rot_{xy}) and point vacancy distribution overlaid on the TEM images, respectively. The white arrows denote the polarization direction within the defect core.

direction, which compresses the nearby vacancy-free regions (Figure 2a–i). In sharp contrast, evident lattice deformation was not observed from the e_{yy} map. From the e_{xy} and rot_{xy} maps, we see a dramatic shear strain and lattice rotation near the defect core, which can be attributed to the structural change caused by atomic polar displacements.

Starting from the initial AFE state, we see that during irradiation of the electron beam, the self-compensated defect core (≈2 nm in diameter) evolves into a dynamic polar structure with local destruction of the antiparallel Pb arrangements (**Figure 3**a–d and Figure S4b–d, Supporting Information). Meanwhile, the defect core initiates an AFD-to-FD transition in a stripe region with width of $\approx b_{AF}$ along x direction, which is characterized by y-direction transformation of oxygen shifts from (0 ↓ 0 ↑)/(0 ↑ 0 ↓) in the AFD state to (0 ↓ ↑ ↑)/(0 ↑ ↓ ↓) in the FD-I state.[14] Herein, the zeros "0" marked by red solid line denote oxygen atoms locating at the centrosymmetric positions. This reveals that polar distortion occurs to the oxygen octahedral in the FD state, which generates a polarization with $P_S \approx 3$ μC cm^{-2} that essentially runs along $[\bar{1}00]_O$ direction according to previous TEM measurement[14] (Figure S2b, Supporting Information). As the irradiation time increases to t = 20 s, the FD-I state expands in unit-cell wise along y direction, which is accompanied with dynamic size change of the defect core.

Clearly, the presence of net polarization in the AFE/AFD-to-FE/FD transition is attributed to storage of electrostatic energy from the electron beam. At t = 35 s, the defect core further induces a new FD-II state. With retaining the FD-I state polarization orientation, the FD-II state is characterized by (0 ↓ ↓ ↑)/(0 ↑ ↑ ↓) oxygen shifts along y direction (Figure 3a and Figure S5a,b, Supporting Information). Accompanied with the structural transition, the polarization forms a partial offset configuration inside the defect core to lower the local electrostatic energy.[32] More interestingly, through reversing the x-direction shift but not the y-direction shift of oxygen, the FD-I state transforms into a new FD-III state, which corresponds to P_S reversal from $[\bar{1}00]_O$ to $[100]_O$ direction. This reveals that the energy storage is accompanied with formation of charged FD domain walls (Figure 3a,g and Figure S5c, Supporting Information). Under continuous irradiation of the electron beam, the injected energy dynamically propagates to nearby regions through motion and density increase of the FD domain walls, which lie in $(100)_O$, $(210)_O$, and $(\bar{2}10)_O$ crystal planes and their width is about one octahedral unit.

Besides changes of the structural order parameters, the lattice parameters from the displayed image area are measured as a function of irradiation time. At the AFE state with t < 0 s, the average lattice parameters are $a_{AF} \approx$ 0.5813 nm,

© 2021 The Authors. Advanced Functional Materials published by Wiley-VCH GmbH

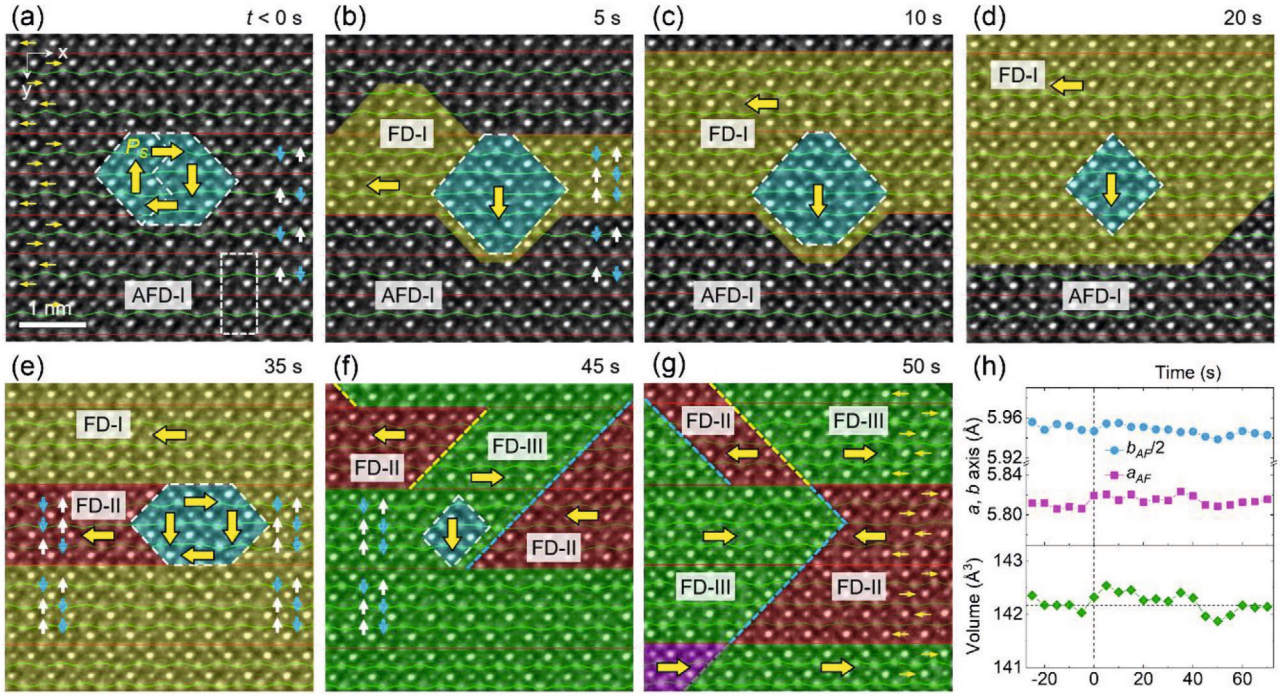

Figure 3. a–g) Evolution of phase and domain structures (yellow, red, green, and purple shadows) near the defect core (cyan region) as a function of electron-beam irradiation time. The polarization (P_S, yellow thick arrows) in the FD states and defect core is determined by mapping oxygen shifts against centers of nearest-neighboring Zr columns (see Figure S5, Supporting Information). The (red, green) solid lines and the (white, blue) arrows highlight the characteristic oxygen displacements along *y* direction. The yellow thin arrows in (a) and (g) denote antiparallel Pb shifts in the AFD and FD states. The white dashed rectangle denotes the AFE unit cell. The yellow and blue dashed lines in (f,g) denote the tail-to-tail and head-to-head charged FE domain walls. h) Evolution of lattice parameters and volume ($V = a_{AF} \times b_{AF} \times c_{AF}/4$) as a function of electron-beam irradiation time.

$b_{AF}/2 \approx 0.5914$ nm and thus the lattice ratio is $b_{AF}/2a_{AF} \approx 1.024$. Referring to the value measured from the SAED pattern, these values of local lattice parameters reveal that the point vacancies near the defect core distort the unit cells at nanometer scale. At $t > 0$ s, the a_{AF} axis slightly increases until $t = 40$ s and the b_{AF} axis continuously decreases (Figure 3a). As a result, the ratio is reduced to $b_{AF}/2a_{AF} = 1.022$. Since the P_S of the FD phase is essentially running along x direction,[14] the reduced lattice ratio (at $t > 0$ s) supports the polarization–strain coupling relation[39] and favors the AFD-to-FD transition. Assuming c_{AF} axis is a constant with $c_{AF}/2 = 4.113$ Å, it can be seen that this phase transition leads to expansion of the unit-cell volume at the initial stage, which is 0.26% at the maximum. Around $t \approx 50$ s, we see that the a_{AF} axis decreases and the unit-cell volume is compressed by about –0.24%. This can be attributed to presence of the head-to-head dipole configuration across the nearly 180° charged domain walls in the FD phase,[40] which take a larger proportion in this local region (Figure 3f,g).

First-principles calculations on $PbZrO_3$ have revealed that the difference in ground-state energy is remarkably small between the FE rhombohedral-like (FE_{RL}) and AFE orthorhombic phases. Of particular interest is that compressive strain obviously favors formation of the FE_{RL} phase.[41,42] Being consistent with the calculation result, our GPA analysis reveals that the defect core is essentially under a compressively strained condition during the dynamic storage process of energy (**Figure 4**a–f). Besides the time-resolved maps, it can also be seen from the extracted line profiles that the e_{xx} values may go down to –30% at the center of the defect core, while the nearby tensile strain is only in the range of ≈3–5% (Figure 4g). This situation remains even when the charged and uncharged FD domain walls were created by the electron-beam irradiation. This indicates that the strain conditions of the defect core (Figures S6 and S7, Supporting Information), governed by distribution and dynamic motion of the point defects, play a decisive role in mediating storage and propagation of the electrostatic energy.

Through quantitative measurements and analyses on the atomic-resolution images, we found that the tilting behavior of oxygen octahedra near the defect core is also affected by polarity evolution of the defect core (Figures S8 and S9, Supporting Information). Associated with minimizing the local energy per unit area, the real-time structural changes of nearby regions suggest that the net polarization of the defect core needs to be compensated dynamically. This implies that the actual size of the defect core is approximately one to three times larger than that delineated in Figure 3. Following the AFD-to-FD transition, further electron-beam irradiation on $PbZrO_3$ instantly transforms the FE/FD phase into the ordinary FE phase.[14]

Together with distribution of the point defects, the shift behavior of oxygen columns relative to centers of the nearest-neighboring Zr columns was mapped and overlaid on the experimental images (**Figure 5**a,b). In the initial ordinary FE state at $t = 80$ s, we see many FE monoclinic (FE_M) nanodomains, which are characteristic of near $[0\bar{1}0]_O$ polarization orientation. After about 1-min irradiation at $t = 135$ s, domains with charged configurations are frequently seen at the nanometer

© 2021 The Authors. Advanced Functional Materials published by Wiley-VCH GmbH

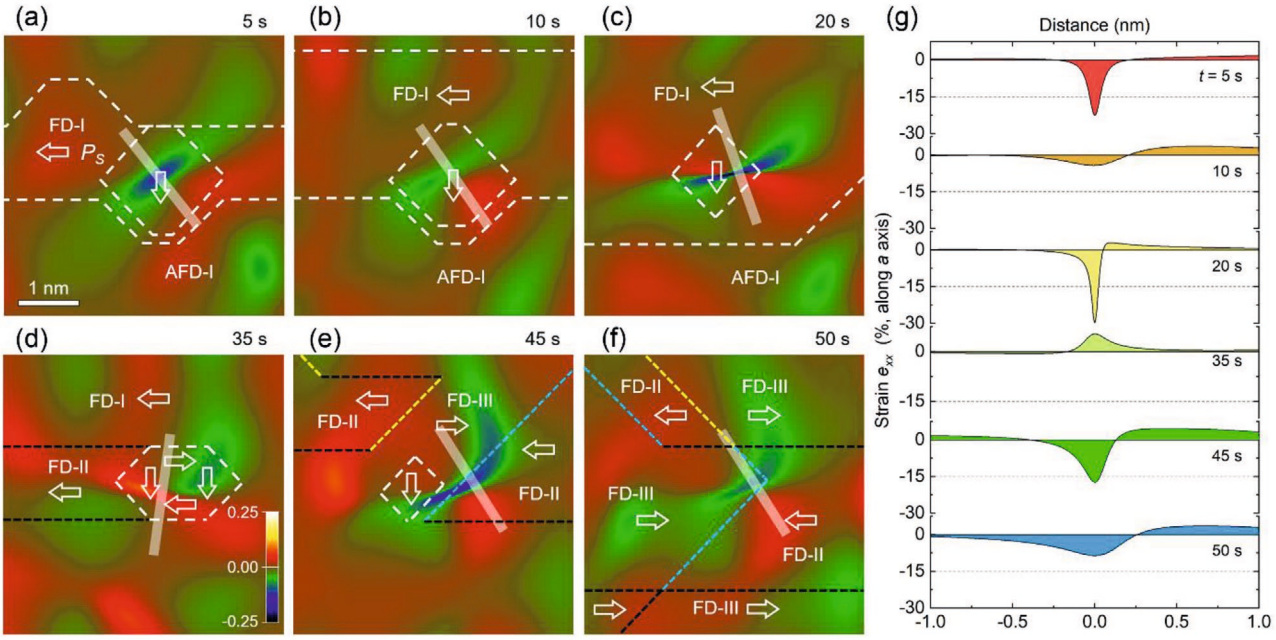

Figure 4. a–f) Maps of e_{xx} lattice strain (along $[100]_O$ direction) obtained from GPA analysis on TEM images shown in Figure 3a–g. The colorful dashed lines denote the phase boundary (white), defect core (white), transversal (black), tail-to-tail (yellow), and head-to-head (blue) charged domain walls between the FD domains, respectively. g) Strain line profiles extracted from the bar-shape regions denoted in the e_{xx} maps shown in (a–f).

scale. As linking to the vacancy distribution, we see that the point defects mainly influence the polarization orientation in the FE_M phase, which is almost ignorable in the FE_R phase. Associated with dynamic transformation between these two phases, the unit-cell-scale FE_R islands are found to embed in the FE_M matrix and grow in size with increase of the irradiation time. This is consistent with proportion change of the FE_M phase ($\phi \approx \pi/2$)[43] and FE_R phase ($\phi = 0$) as a function of irradiation time (Figure 5c–f).

Previous studies have reported that the spontaneous polarization is $P_S \approx 32$ and 55 μC cm^{-2} for the FE_M and FE_R phase, respectively.[14,44] This indicates that the FE_M-to-FE_R transition

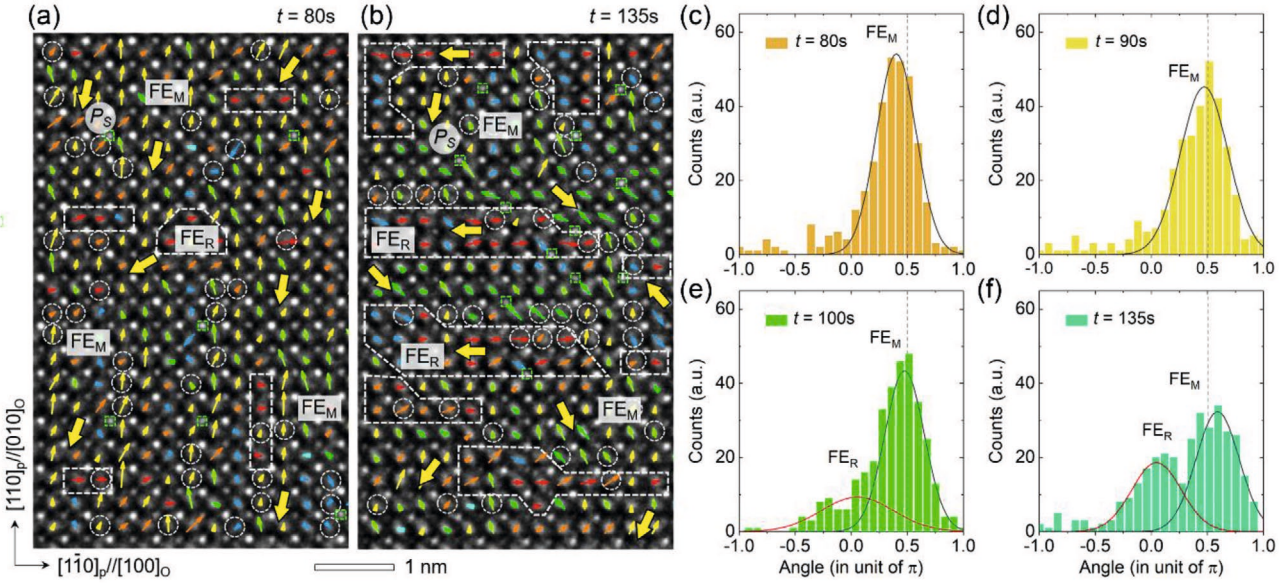

Figure 5. a,b) Atomic-resolution TEM images of ordinary FE phases recorded at $t = 80$ and 135 s along the $[001]_O$ direction. The oxygen displacement maps (color arrows) against centers of the nearest-neighboring Zr columns and representative P_S orientation of nanodomains (yellow thick arrows, projected on the $[001]_O$ plane) are overlaid on the images. The white dashed polygons denote the FE_R islands against the FE_M matrix. The white dashed circles and green dashed squares denote oxygen and Pb columns with certain concentration of point vacancy. c–f) Statistical angle analysis of oxygen displacements as a function of electron-beam irradiation time. The angles for the FE_M phase and FE_R phase are at $\phi \approx \pi/2$ and $\phi = 0$, respectively.

© 2021 The Authors. Advanced Functional Materials published by Wiley-VCH GmbH

allows further storage of the electrostatic energy by further irradiation of the electron beam, which is accompanied with FE_M domain reorientation and growth of the FE_R domains (Figure S10, Supporting Information). Presence of the high-energy and metastable charged domain walls[45,46] can be understood as a way of temporally storing the injected energy, which may propagate to nearby regions subsequently and the collected charges can be evaluated by $Q(t) = \int_0^t i(t)\,dt$, with i being the stored electric current at a given time t.[47,48] At this stage, the unit-cell-wise FE_M-to-FE_R transition takes place as well (see Figure S11, Supporting Information). Nevertheless, regular domain structure change was not observed due to flexible P_S rotation within certain crystal plane of the FE_M phase,[32] high similarity in lattice parameters,[43] and closeness in free energy between these two phases.[49] Relating to the point vacancy distribution, our GPA analysis shows that the initial defect core is dismembered at the ordinary FE states (Figure S12, Supporting Information).

As for the driving force of the phase transitions, the following facts suggest that this is dominated by charging effect combined with kinetic energy transfer of the electron beam. For the charging effect, a direct evidence is the random shaking of the specimen under electron-beam irradiation inside the microscope, which plays a key role in triggering the stepwise AFD-to-FD transition (Figure S13, Supporting Information). Although occurrence of the phase transition is accompanied with negative electrocaloric effect,[50] a nearly constant magnitude of the Pb-atom antiparallel displacement, in the range of ≈18–20 pm, and the shrinking tendency of unit-cell volume with time indicate that the contribution of heating effect is ignorable, which leads to gradual decrease of Pb displacement with increasing temperature.[51] With weakening of the charging effect, the kinetic energy transfer through inelastic scattering of electrons drives the subsequent phase transitions in the specimen. This is manifested by the dramatic increase of polarization during the FD-to-ordinary FE state transition.

Regarding the structural phases observed in $PbZrO_3$, the soft-mode theory of phase transition gives a clear classification and interpretation.[52] Usually, the AFD order arises from a mode condensation at the Brillouin zone boundary and leads to unit-cell doubling. As it couples with a polar mode with null polarization, an AFE order emerges in the orthorhombic phase. Instead, the FD order is triggered by condensation of a zone-center soft mode. In this sense, the AFE and FE transitions are subgroups of AFD and FD transitions, respectively. Nevertheless, the AFD order may also couple with a net polarization, for example, in the FE_R ($R3c$) phase with $a^-a^-a^-$-type octahedral rotations. For the FE_M (Cm) phase with $a^0a^0a^0$-type rotations,[43] there is only zone-center mode condensation. As for the effect of point defects, one can see that it breaks local crystallographic symmetry and introduces local chemical pressure and local polarization, as reported in HfO_2.[53,54] Relative to the capacitor geometry, despite different driving forces, the phase-transition mechanisms[4,5] are expected to be similar given the pinning effect of structural defects and interfaces to electric polarization.[18,19] In addition, the increase of P_r induced by neutron irradiation dose in $PbZrO_3$ suggests that the mechanism reported here may extend to bulk ceramics.[12,55]

3. Conclusions

In summary, benefiting from slowing down the energy-storage process using electron-beam irradiation, our in situ atomic-resolution TEM study reveals that the point defects play as seeds to initiate the AFE/AFD-to-FE/FD transition. Starting from the vacancy-induced defect core, featured by local compressive strain and polar instability, the AFE/AFD state is stepwisely transformed into the FE/FD state via generation of domain stripes with variable width at unit-cell scale. Specifically, we found formation of charged domain walls at different FE states, which reflects the way of temporally storing injected energy before spreading to nearby regions. Given that proper defect concentration may improve the breakdown electric field and thus U_e,[12,24] it is believed that our findings offer insights to optimize performances, and open up a pathway to configure atomic-scale structure–property relationship in chemical defect-engineered energy storage dielectrics.

4. Experimental Section

Material Preparation: The $PbZrO_3$ single crystals were grown by flux method with the $PbO–B_2O_3$ mixture (soaking at 1300 K) used as a solvent. Details about the cooling procedures and removal of the residuals were presented elsewhere.[18] The lamella specimens were prepared using an FEI Helios Nanolab 400s focused ion beam system. After removal of the contamination and damaged layers using NanoMill Model 1040 system, which was operated at 500 V, the lamella samples were heated above T_C and then cooled down to room temperature at a rate of ≈9 K min^{-1}. By repeating this procedure several times, the point vacancy defects were introduced into the lamella specimens.

Imaging Experiments: The domain structure analysis and SAED experiments were carried out on an FEI Tecnai F20 microscope. The atomic-resolution TEM experiments were performed on an FEI Titan 80–300 microscope, which was equipped with a *Cs* corrector for the objective lens and was operated at an accelerating voltage of 300 kV. The available point resolution was better than 80 pm and a dose rate of the electron beam was ≈3.8×10^6 e·nm^{-2}·s^{-1}. A 2k × 2k Gatan UltraScan 1000 CCD camera was used for the image acquisition and each frame exposure time was 0.8 s. Structure modeling and multislice-based image simulation were carried out using the CrystalKit-MacTempas software package. The parameters used for simulating the images were C_S = –12 µm, $A1$ = 2.5 nm, $A2$ = 3 nm, and $B2$ = 3 nm. The lattice parameters of the image area were measured and averaged by mapping positions of the Zr columns.

Image Measurement and Quantification: In the authors' experiments, the quantitative measurement and analysis were carried out on as-obtained high quality TEM images, in which the atomic column peak intensities were fitted by 2D Gaussian function based on maximum-likelihood estimation.[35] Since the antiparallel Pb displacements were compensated in the AFE/AFD and FE/FD phases,[14] the centrosymmetric lattice origin was defined by symmetrizing Pb displacements along the $x/[100]_O$ and $y/[010]_O$ direction.

Supporting Information

Supporting Information is available from the Wiley Online Library or from the author.

Acknowledgements

X.-K.W. acknowledges support by the Deutsche Forschungsgemeinschaft (DFG; German Research Foundation) under Germany's Excellence

© 2021 The Authors. Advanced Functional Materials published by Wiley-VCH GmbH

Strategy-Cluster of Excellence Matter and Light for Quantum Computing (ML4Q) EXC 2004/1-390534769. The authors thank D. Meertens for sample preparation.

Open access funding enabled and organized by Projekt DEAL.

Conflict of Interest

The authors declare no conflict of interest.

Keywords

charged domain walls, energy storage, ferrodistortive transition, in situ transmission electron microscopy, $PbZrO_3$

Received: October 9, 2020
Revised: December 4, 2020
Published online: January 14, 2021

[1] H. Palneedi, M. Peddigari, G.-T. Hwang, D.-Y. Jeong, J. Ryu, *Adv. Funct. Mater.* **2018**, *28*, 1803665.
[2] H. Pan, F. Li, Y. Liu, Q. W. Zhang, S. L. Meng, Y. Zheng, J. Ma, L. Gu, Y. Shen, P. Yu, S. Zhang, L.-Q. Chen, Y.-H. Lin, C.-W. Nan, *Science* **2019**, *365*, 578.
[3] J. Li, Z. Shen, X. Chen, S. Yang, W. Zhou, M. Wang, L. Wang, Q. Kou, Y. Liu, Q. Li, Z. Xu, Y. Chang, S. Zhang, F. Li, *Nat. Mater.* **2020**, *19*, 999.
[4] B. Xu, J. Iniguez, L. Bellaiche, *Nat. Commun.* **2017**, *8*, 15682.
[5] S. Lisenkov, Y. Yao, N. Bassiri-Gharb, I. Ponomareva, *Phys. Rev. B* **2020**, *102*, 104101.
[6] C. T. Blue, J. C. Hicks, S. E. Park, S. Yoshikawa, L. E. Cross, *Appl. Phys. Lett.* **1996**, *68*, 2942.
[7] Y. Cai, F. Phillipp, A. Zimmermann, L. Zhou, F. Aldinger, M. Rühle, *Acta Mater.* **2003**, *51*, 6429.
[8] H. He, X. Tan, *Phys. Rev. B* **2005**, *72*, 024102.
[9] B. Chu, X. Zhou, K. Ren, B. Neese, M. Lin, Q. Wang, F. Bauer, Q. M. Zhang, *Science* **2006**, *313*, 334.
[10] X. Tan, C. Ma, J. Frederick, S. Beckman, *J. Am. Ceram. Soc.* **2011**, *94*, 4091.
[11] H. Wang, Y. Liu, T. Yang, S. Zhang, *Adv. Funct. Mater.* **2019**, *29*, 1807321.
[12] X. Liu, Y. Li, N. Sun, X. Hao, *Inorg. Chem. Front.* **2020**, *7*, 756.
[13] T. Zhang, Y. Zhao, W. Li, W. Fei, *Energy Storage Mater.* **2019**, *18*, 238.
[14] X. K. Wei, C. L. Jia, H. C. Du, K. Roleder, J. Mayer, R. E. Dunin-Borkowski, *Adv. Mater.* **2020**, *32*, 1907208.
[15] H. Zheng, J. B. Rivest, T. A. Miller, B. Sadtler, A. Lindenberg, M. F. Toney, L.-W. Wang, C. Kisielowski, A. P. Alivisatos, *Science* **2011**, *333*, 206.
[16] B. K. Mani, C. M. Chang, S. Lisenkov, I. Ponomareva, *Phys. Rev. Lett.* **2015**, *115*, 097601.
[17] C. L. Jia, L. Houben, A. Thust, J. Barthel, *Ultramicroscopy* **2010**, *110*, 500.
[18] X.-K. Wei, A. K. Tagantsev, A. Kvasov, K. Roleder, C.-L. Jia, N. Setter, *Nat. Commun.* **2014**, *5*, 3031.
[19] X.-K. Wei, Y. Yang, L. J. McGilly, L. Feigl, R. E. Dunin-Borkowski, C.-L. Jia, L. Bellaiche, N. Setter, *Phys. Rev. B* **2018**, *98*, 020102(R).
[20] X. Hao, J. Zhai, L. B. Kong, Z. Xu, *Prog. Mater. Sci.* **2014**, *63*, 1.
[21] T. Ma, Z. Fan, B. Xu, T.-H. Kim, P. Lu, L. Bellaiche, M. J. Kramer, X. Tan, L. Zhou, *Phys. Rev. Lett.* **2019**, *123*, 217602.
[22] Z. Fu, X. Chen, Z. Li, T. Hu, L. Zhang, P. Lu, S. Zhang, G. Wang, X. Dong, F. Xu, *Nat. Commun.* **2020**, *11*, 3809.
[23] S. Li, H. Nie, G. Wang, C. Xu, N. Liu, M. Zhou, F. Cao, X. Dong, *J. Mater. Chem. C* **2019**, *7*, 1551.
[24] N. Luo, K. Han, F. Zhuo, C. Xu, G. Zhang, L. Liu, X. Chen, C. Hu, H. Zhou, Y. Wei, *J. Mater. Chem. A* **2019**, *7*, 14118.
[25] H. Qi, R. Zuo, A. Xie, A. Tian, J. Fu, Y. Zhang, S. Zhang, *Adv. Funct. Mater.* **2019**, *29*, 1903877.
[26] K. Roleder, J. Dec, *J. Phys.: Condens. Matter* **1989**, *1*, 1503.
[27] X.-K. Wei, C.-L. Jia, K. Roleder, N. Setter, *Mater. Res. Bull.* **2015**, *62*, 101.
[28] X.-K. Wei, K. Vaideeswaran, C. S. Sandu, C.-L. Jia, N. Setter, *Adv. Mater. Interfaces* **2015**, *2*, 1500349.
[29] V. I. Arkhipox, A. I. Rudenko, G. M. Sessier, *J. Phys. D: Appl. Phys.* **1993**, *26*, 1298.
[30] R. F. Egerton, P. Li, M. Malac, *Micron* **2004**, *35*, 399.
[31] C. L. Jia, M. Lentzen, K. Urban, *Science* **2003**, *299*, 870.
[32] X.-K. Wei, C.-L. Jia, T. Sluka, B.-X. Wang, Z.-G. Ye, N. Setter, *Nat. Commun.* **2016**, *7*, 12385.
[33] D. L. Corker, A. M. Glazer, J. Dec, K. Roleder, R. W. Whatmore, *Acta Crystallogr., Sect. B: Struct. Sci., Cryst. Eng. Mater.* **1997**, *53*, 135.
[34] K. Yamasaki, Y. Soejima, K. F. Fischer, *Acta Crystallogr., Sect. B: Struct. Sci., Cryst. Eng. Mater.* **1998**, *54*, 524.
[35] R. Parthasarathy, *Nat. Methods* **2012**, *9*, 724.
[36] V. Stepkova, P. Marton, N. Setter, J. Hlinka, *Phys. Rev. B* **2014**, *89*, 060101.
[37] Y. Nahas, S. Prokhorenko, L. Bellaiche, *Phys. Rev. Lett.* **2016**, *116*, 117603.
[38] M. J. Hÿtch, E. Snoeck, R. Kilaas, *Ultramicroscopy* **1998**, *74*, 131.
[39] T. Qi, I. Grinberg, A. M. Rappe, *Phys. Rev. B* **2010**, *82*, 134113.
[40] C. L. Jia, S. B. Mi, K. Urban, I. Vrejoiu, M. Alexe, D. Hesse, *Nat. Mater.* **2008**, *7*, 57.
[41] S. E. Reyes-Lillo, K. M. Rabe, *Phys. Rev. B* **2013**, *88*, 180102.
[42] H. Fujishita, Y. Shiozaki, E. Sawaguchi, *J. Phys. Soc. Jpn.* **1979**, *46*, 1391.
[43] H. Yokota, N. Zhang, A. E. Taylor, P. A. Thomas, A. M. Glazer, *Phys. Rev. B* **2009**, *80*, 104109.
[44] R. Kagimura, D. Singh, *Phys. Rev. B* **2008**, *77*, 104113.
[45] T. Sluka, A. K. Tagantsev, P. Bednyakov, N. Setter, *Nat. Commun.* **2013**, *4*, 1808.
[46] X. K. Wei, T. Sluka, B. Fraygola, L. Feigl, H. Du, L. Jin, C. L. Jia, N. Setter, *ACS Appl. Mater. Interfaces* **2017**, *9*, 6539.
[47] A. I. Khan, K. Chatterjee, B. Wang, S. Drapcho, L. You, C. Serrao, S. R. Bakaul, R. Ramesh, S. Salahuddin, *Nat. Mater.* **2015**, *14*, 182.
[48] P. Maksymovych, S. Jesse, P. Yu, R. Ramesh, A. P. Baddorf, S. V. Kalinin, *Science* **2009**, *324*, 1421.
[49] J. A. Rodriguez, A. Etxeberria, L. Gonzalez, A. Maiti, *J. Chem. Phys.* **2002**, *117*, 2699.
[50] P. Vales-Castro, R. Faye, M. Vellvehi, Y. Nouchokgwe, X. Perpinà, J. M. Caicedo, X. Jordà, K. Roleder, D. Kajewski, A. Perez-Tomas, E. Defay, G. Catalan, *arXiv:2009.02184*, **2020**.
[51] R. W. Whatmore, A. M. Glazer, *J. Phys. C: Solid State Phys.* **1979**, *12*, 1505.
[52] M. E. Lines, A. M. Glass, *Principles and Applications of Ferroelectrics and Related Materials*, Oxford University Press, Oxford **2001**.
[53] X. Sang, E. D. Grimley, T. Schenk, U. Schroeder, J. M. LeBeau, *Appl. Phys. Lett.* **2015**, *106*, 162905.
[54] M. D. Glinchuk, A. N. Morozovska, A. Lukowiak, W. Stręk, M. V. Silibin, D. V. Karpinsky, Y. Kim, S. V. Kalinin, *J. Alloys Compd.* **2020**, *830*, 153628.
[55] R. Bittner, K. Humer, H. W. Weber, K. Kundzins, A. Sternberg, D. A. Lesnyh, D. V. Kulikov, Y. V. Trushin, *J. Appl. Phys.* **2004**, *96*, 3239.

© 2021 The Authors. Advanced Functional Materials published by Wiley-VCH GmbH